FINAL TECHNICAL REPORT

AWARD NUMBER: 02HQGR0066

TITLE: Mapping and characterizing active faults using sub-triggering-threshold earthquakes

AUTHOR:
Allan Rubin
Department of Geosciences
Princeton University
Princeton, NJ 08544

Telephone: (609) 258-1506
Fax: (609) 256-1274
email: arubin@princeton.edu

TERM: 02/01/2002-01/31/2004

ABSTRACT

We examined the waveforms of over 2,000 centrally-located earthquakes from the HRSN borehole network near Parkfield, CA, to search for immediate aftershocks that were buried in the mainshock coda and that therefore passed undetected by the network triggering algorithm. Each event was deconvolved using as empirical Green functions the 5 catalog events to which it was most similar. Using this technique 30 earthquakes were identified as either compound earthquakes or mainshock/aftershock pairs. Ten of these had inter-event delay times of less than 15 ms, with the second event plausibly occurring at the tail end of the dynamic phase of the mainshock. Of this latter group, nearly all the triggered events occurred to the NW of the mainshock. We compared this result to the predictions of elastodynamic models of ruptures on an interface separating differing elastic materials (a bimaterial interface) in an effort to better constrain how such an interface influences the rupture dynamics. Understanding this is relevant to hazards analysis because such interfaces may promote consistent rupture directivity and hence systemmatically stronger ground shaking in one direction than another, but this proposal remains controversial.

INTRODUCTION

Events that lie below the detection level of standard network triggering algorithms represent a potential wealth of data regarding fault zone structure and mechanics. This is made possible because earthquake relocation using waveform cross-correlation typically provides relative location errors that are a small fraction of the earthquake diameters. We report here on a study to apply such techniques to earthquakes buried in the codas of archived earthquakes recorded by the HRSN borehole seismic network near Parkfield, CA. These "second events" can be thought of straddling the transition between very early aftershocks and sub-events in compound earthquakes. A working definition of this transition is whether the stress changes due to the mainshock, evaluated at the origin time and location of the second event, had reached their final quasi-static value (in which case the second event is an aftershock) or were still strongly time-varying (in which case the second event was a subevent in a compound earthquake). The goal was to better characterize the mechanics of earthquake rupture on a bimaterial interface.

The primary observational motivation for this work is shown in Figure 1. The left panel shows the stacked aftershock sequences of 5,000 M1-M3 earthquakes located near the northern end of the creeping section of the San Andreas fault [Rubin, 2002]. Each earthquake is successively placed at the origin, and the relative locations of all relocated earthquakes occurring within the next 10 hours are projected onto the fault surface, after normalizing by the estimated radius of the first (assuming circular ruptures, 10-MPa stress drops, and the moment-magnitude relation of Abercrombie [1996]). Within 2 radii the distribution is decidedly asymmetric. Of the 169 aftershocks beyond the mode-II edges of the mainshock (those with relative position vectors within 45^o of horizontal),

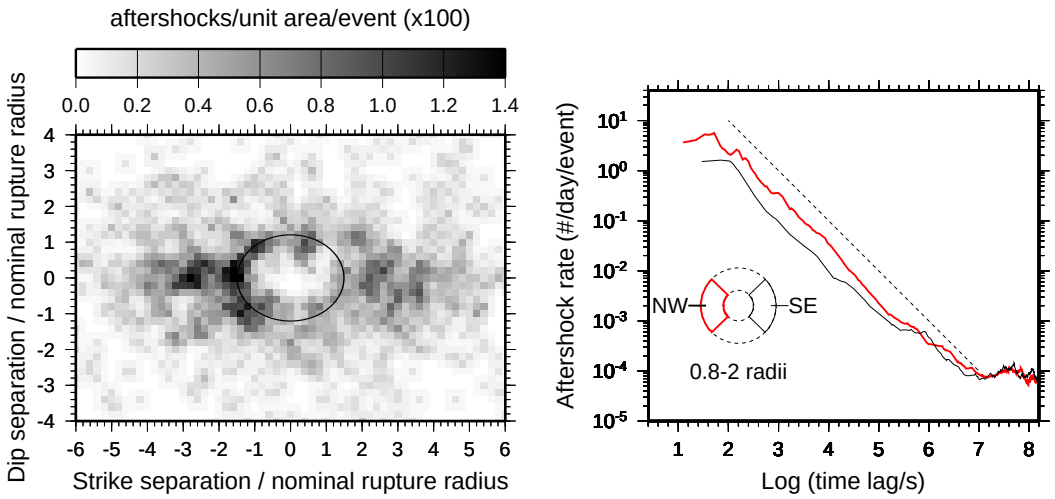

Figure 1: (left) Stacked aftershock sequences of 5,000 microearthquakes along 60 km of the San Andreas fault near San Juan Bautista, from Rubin [2002]. The ellipse, symmetric about the origin, is drawn to pass through the high-density region of aftershocks to the NW and at the mode-III margins and corresponds to a stress drop of 4.5 MPa. The asymmetry is restricted to about 2 earthquake radii. (right) Seismicity rate as a function of time following the composite mainshock, for aftershocks from 0.8-2 estimated radii to the NW (red) and SE (black), showing the factor of $\sim$3 difference at early times and the near symmetry for time delays $\gtrsim 10^6$ s (10 days). The dashed line shows a decay rate of 1/time.

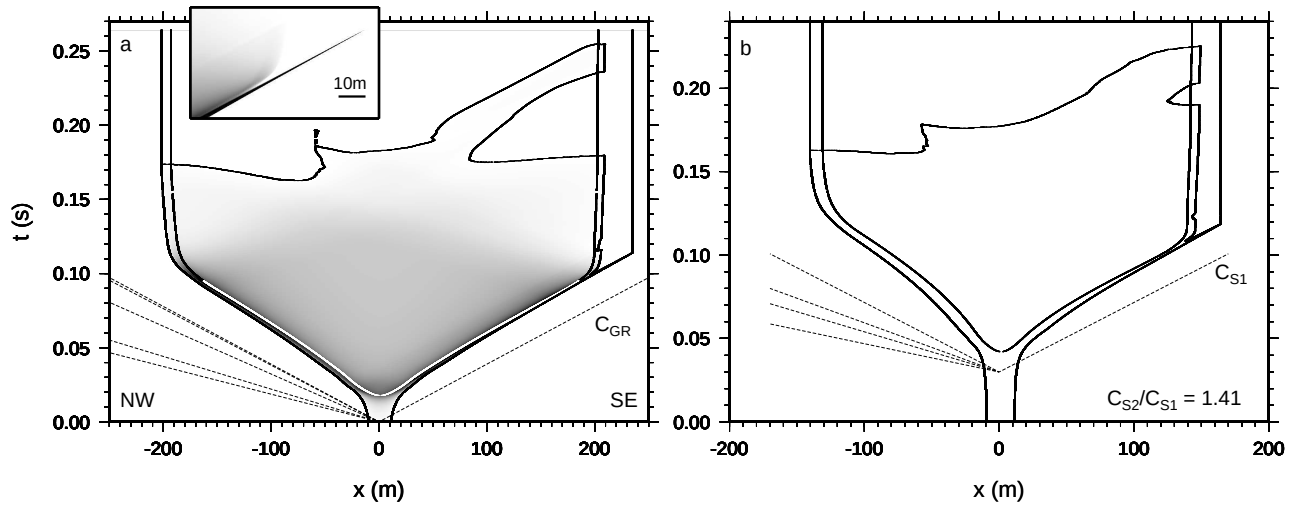

Figure 2: Numerical simulations of ruptures on a bimaterial interface. (a) Slip speed as a function of space and time for a shear wave speed contrast C_{S2}/C_{S1} of 1.18, with shear stress barriers of 0.2 MPa/m placed at $\pm$160 m. The speed limit for propagation of the SE rupture front (the front moving in the direction of slip of the more compliant material) is the generalized Rayleigh speed C_{GR}. Grayscale image of the slip saturates at 2 m/s; peak velocity is 10 m/s. The outermost lines represent the rupture front; inner lines the tail end of the slip weakening region. Also shown are the contours of zero slip speed. Inset shows an enlargement of the pulse at the SE front. Dashed lines indicate (from fastest to slowest) C_{P2}, C_{P1}, C_{S2}, C_{S1}, and C_{GR}. (b) The same plots for $C_{S2}/C_{S1} = 1.41$. For velocity contrasts this large C_{GR} does not exist; the limiting speed for subshear ruptures is then C_{S1}. From Rubin and Ampuero [2007].

125 occurred to the NW and 44 to the SE. In a coin-toss such lopsided statistics have a probability of occurrence of 1 in 10^9. In contrast, beyond the mode-III ends of the mainshock, 61 aftershocks were shallower and 64 deeper. The right panel shows the time-dependence of the aftershock rates in the region where the asymmetry is most pronounced (roughly 1-2 radii). The seismicity rate of the stacked aftershock sequence decays as nearly 1/time to a quasi-uniform background rate. Significantly, there is no asymmetry of the background, and little or none after about 1 day ($\sim 10^5$ s).

For a planar fault in a homogeneous body there is no obvious mechanism for producing such asymmetry. However, for the San Andreas and other large crustal faults, large displacements have juxtaposed rocks of differing mechanical properties. This breaks the symmetry at the mode-II margins but not the mode-III margins of the rupture, consistent with the observations. The velocity contrast across the SAF in this region is as large as 35% [McGuire and Ben Zion, 2005], with lower-velocity rock lying to the NE. Significantly, we see no aftershock asymmetry across the Calaveras fault [Rubin, 2002], which from our cross-correlation delay measurements has a negligible across-fault velocity contrast.

Weertman [1980] showed analytically that for steadily-propagating ruptures there is a (potentially large) tensile stress perturbation behind rupture fronts moving in the direction of motion of the more compliant medium (North America, moving to the SE, in the context of the San Andreas). Our numerical simulations suggested two possible explanations for the observed aftershock asymmetry. First, as the SE-propagating rupture front encounters a barrier and slows down, the tensile stress perturbation continues down the fault and carries a dying slip pulse with it (Figure 2). This

slip pulse smooths the stress field and lowers the stress concentration at the SE front relative to that at the NW. Moreover, because the tensile pulse that carried the slip pulse is a transient dynamic feature, after motion has ceased the SE rupture front is left far below the failure threshold. In contrast, the NW rupture front slows gradually and stops much as it would in a homogeneous medium (Figure 2), leaving the NW rupture front essentially at the failure threshold after slip ceases.

The second possibility is that the dynamic tensile pulse that continues down the fault "depopulates" that region of potential aftershocks by making them part of the mainshock. To distinguish between these mechanisms we need accurate relative timing and location of the earliest aftershocks, triggered not long after the arrival time of the shear stress front. This is not a trivial task because the seismograms of such events overlap.

DATA ANALYSIS

We used the triggered waveform archive of the Parkfield High-Resolution Seismic Network (HRSN) for the period 1987-1998. The network has 10 3-component borehole stations of intermediate depth, recording at 500 Hz. This region also has a large velocity contrast across the fault [Thurber et al., 2006]. We chose to work with this dataset rather than the NCSN data of Figure 1 because the signal-noise ratio is much greater, with with high seismogram coherency up to 80 Hz. This advantage is offset slightly by the generally smaller earthquake magnitudes, which requires greater absolute accuracy in the relative locations when investigating earthquake interaction. The 2300 events and station locations are indicated in Figure 3.

The seismograms we sought to identify appear as the superposition of two discrete but highly similar waveforms offset by a small fraction of the P- to S-wave delay time at the recording stations.

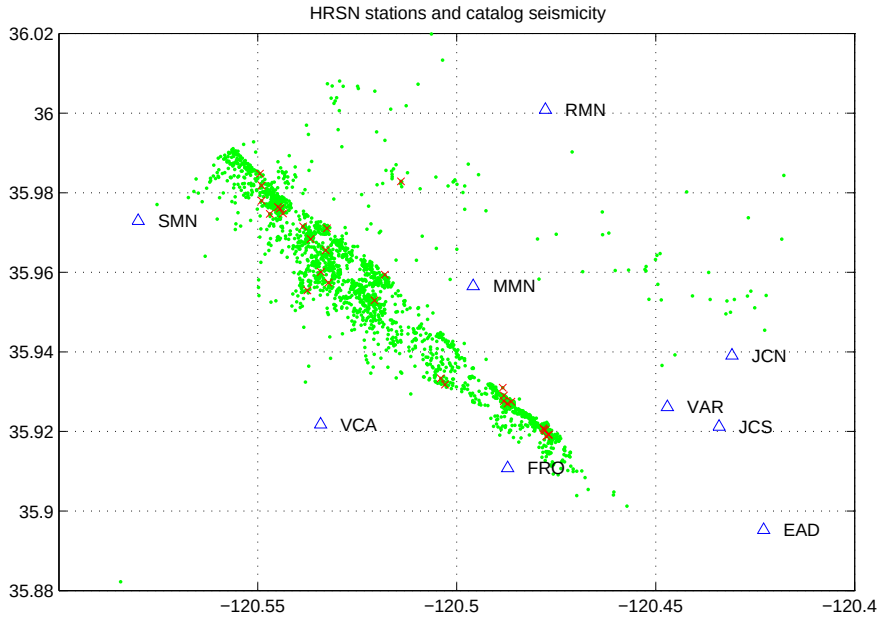

Figure 3: Map showing station locations (blue triangles), earthquakes (green dots), and identified compound seismograms (red crosses).

The high degree of similarity is due to the close proximity of the two events and their (presumably) similar focal mechanisms. In general terms, we deconvolved each earthquake by its 5 most similar earthquakes in the catalog, as measured by cross-correlation, and sought source-time functions that had two (or more) distinct peaks at multiple channels and multiple stations across the network. The delays between these peaks were then used to obtain relative locations and origin times for the two events. For a recording system operating at 500 Hz, P-waves that travel at 5 km/s move 10 m in one sample. This is probably a typical rupture dimension for the small (mostly $M < 1$) earthquakes in this dataset. Therefore we needed to measure the relative delay times of superimposed events with accuracies that were better than 1 sample. This placed quite stringent demands on the data analysis techniques, and required the development of new data-processing strategies. Some details are listed below.

Step 1: Empirical Green's Function (EGF) selection:

For interevent time lags ΔT of less than a few samples EGFs can be selected by coherency. However, coherency degrades around frequencies $f_n = n/\Delta T$ due to destructive interference. In principle, if events 1 and 2 have similar EGFs, the components x and y of their seismograms should be related by:

$$S_x^1 * S_y^2 = S_x^2 * S_y^1$$

So for longer ΔT, optimal EGFs are selected by multi-component convolution coherency.

Step 2: Iterative deconvolution:

We apply the Landweber deconvolution method to determine the source-time functions (STFs) of the target earthquakes. This is $\sim$100 times slower than spectral division but avoids wrap-around effects (we use short time windows) and allows for the introduction of positivity constraints. Figure 4 shows a target earthquake/EFG pair at 8 stations (left column) and the resulting STF of the target (right column). Note the high degree of similarity between the two earthquakes, despite the fact that the target is composed of two near-occurrences of the EGF separated by about 0.1 s (the compound nature of the target is best seen in the raw data at station JCN).

Step 3: Multichannel subevent detection:

The resulting STFs are scanned for significant peaks, defined as outliers among local maxima. To minimize spurious detection due to sidelobes and ringing of the STFs, a threshold of 5 is applied to the number of channels detecting a significant peak in sliding windows of 10 samples. Candidate compound events are visually inspected before further processing. An example is shown in Figure 5.

Step 4: Subevent delays by waveform fit:

Subsample-precision picking of subevents is attempted, for each channel, by waveform fitting. Assuming double sources,

$$S(t) = a_1\, E(t - t_1) + a_2\, E(t - t_2)$$

where $S(t)$ is the seismogram of the compound target event, $E(t)$ is the EGF seismogram, t_1 and t_2 are the apparent times of the first and second occurrences of the EGF within the target, and a_1 and a_2 are their amplitudes. t_1 and t_2 were obtained by grid search and a_1 and a_2 by linear inversion.

Step 5: Relative locations:

We make use of take-off vectors from the 3D velocity model of Thurber et al. [2006].

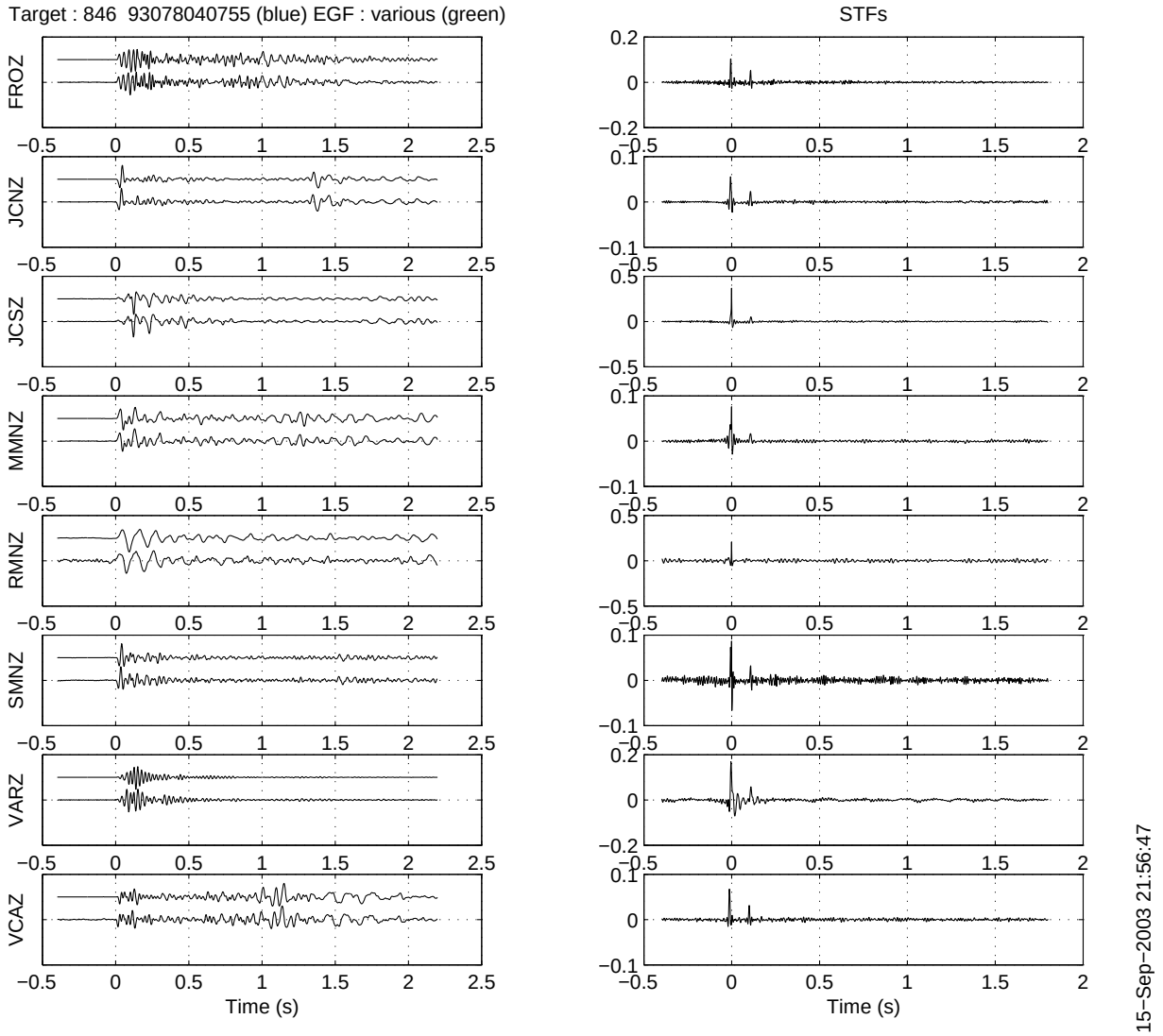

Figure 4: Left column: A target event (2nd trace) and its EGF event (top trace) as recorded on the vertical components of 8 stations. Right column: The STF determined for the target by deconvolution. Note the second peak at $\sim$0.2 s.

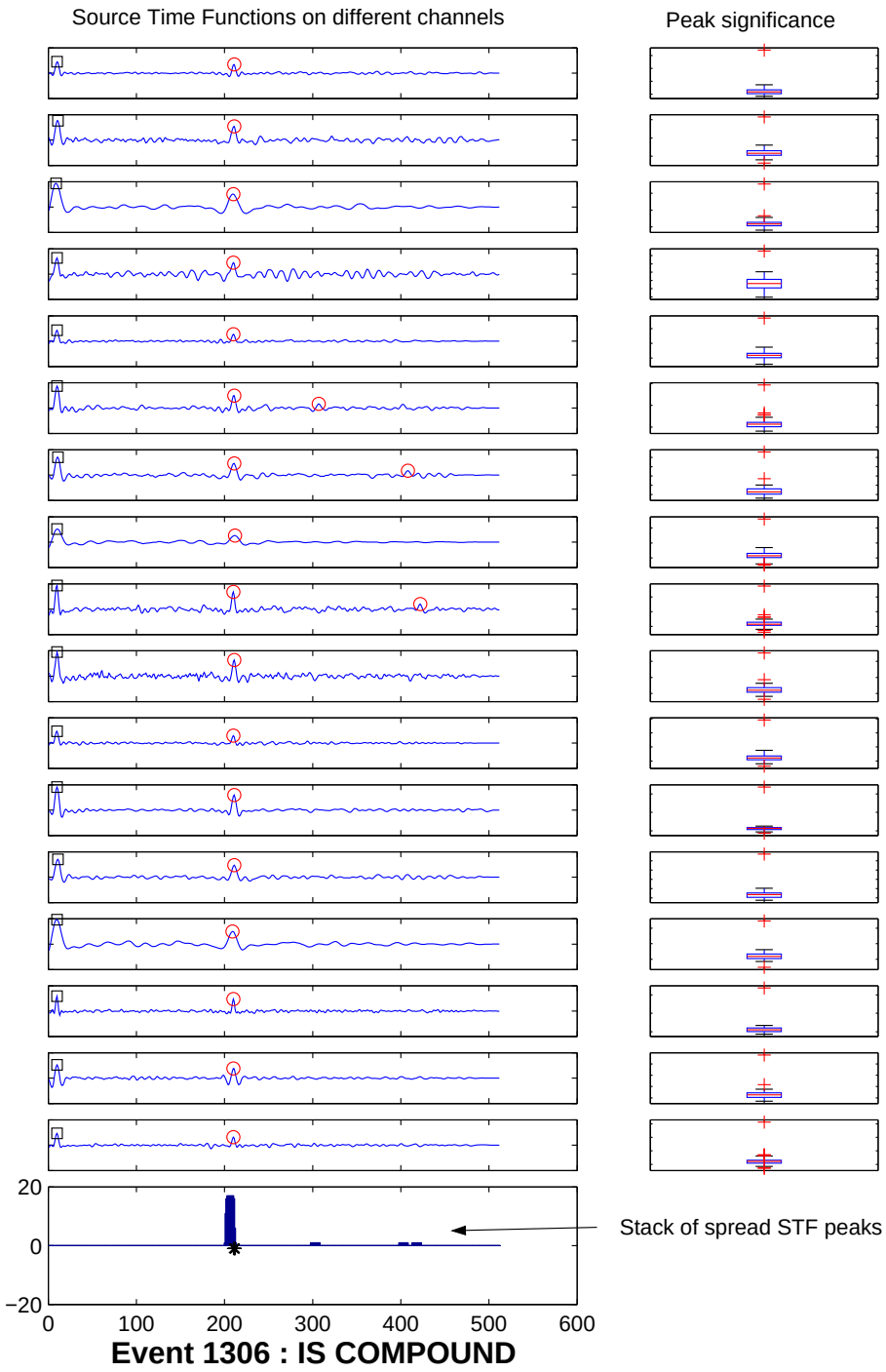

Figure 5: Example of a compound event detection. Left column: The STFs determined for 17 channels, and (bottom) the stack of all 17 STFs. The square indicates the first occurrence of the EGF (the mainshock), and the red circles potential second occurrences of the EGF. Right column: The significance of the amplitude of the STF at all the red circles, as determined by comparison to all the peaks in the STF. Anything lying above the blue brackets lies within the top quartile of "detections" for that channel. The detection at ∼200 ms is clearly significant.

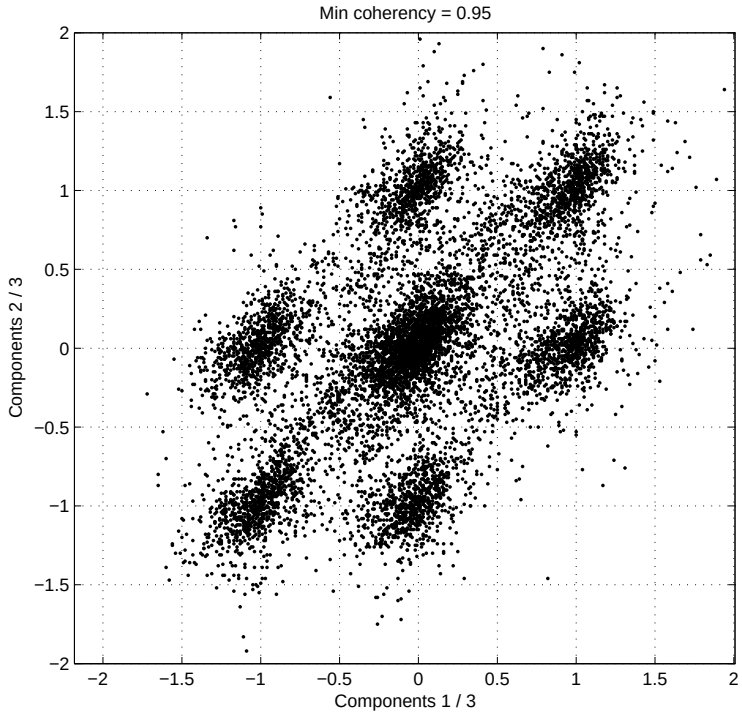

Figure 6: The difference in P- or S-wave delay measurements between similar earthquakes as measured on components 2 and 3 (vertical axis) and components 1 and 3 (horizontal axis). The discrete nature of the delay differences, which if due only to cross-corellation error should all cluster near the origin, is due to the asynchronous station clocks and the 1/3-sample shift between the different components.

RESULTS

Catalog earthquake locations and aftershock asymmetry

The first step was to obtain relative locations for the catalog events, as in Figure 1. Here we found that the gain of sub-sample precision from the cross-spectral delay measurements was counterbalanced by the 1-sample uncertainty due to the use of asynchronous station clocks. Figure 6 compares the difference between delays for similar events measured on different components and shows the discreteness of these timing errors. We are working towards tracking the discrete $1/3$-sample shifts and exploiting them to correct for station clock drifts (leading ultimately to $\pm 1/3$ sample, rather than ± 1 sample, uncertainty).

To circumvent this shortcoming of the data we looked instead to Felix Waldhauser's relocated catalog from Parkfield [Thurber et al., 2006]. Figure 7 indicates that aftershock asymmetry there is of opposite sign to that in Figure 1. Because the large-scale across-fault velocity contrast is of the same sense, this is unexpected. The time window that maximizes the asymmetry is comparable to that in Figure 1; Figure 7 shows a 1-day window. The asymmetry is considerably less than that in Figure 1 ($< 60\%$ more to the SE, out to 2 or 2.5 radii, compared to $> 180\%$ more to the NW in Figure 1), and unlike Figure 1 it is not obvious that the seismicity rate on the side with the aftershock deficit peaks at larger distances than 1-2 radii. Nonetheless, the asymmetry is fairly

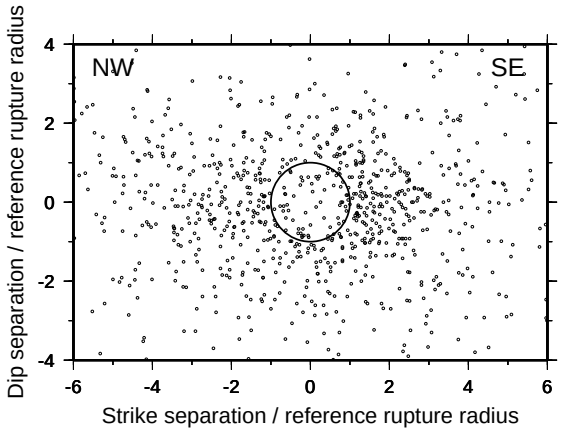

Figure 7: Stacked aftershock sequences of 5,700 microearthquakes along 60 km of the San Andreas fault near Parkfield, 1984-2004, from Felix Waldhauser's catalog [Thurber et al., 2006]. The increased scatter relative to Figure 1 may be due to the lack of time-dependent station delays [Rubin, 2002b]. The circle is for a mainshock stress drop of 10 MPa.

consistent along strike and with depth, and again there is no significant asymmetry above or below the mainshock ($\sim$15% more aftershocks occur below). One way out of this dilemma might be the suggestion by Rudnicki and Rice [2006] that contrasting poroelastic and permeability properties may be as important as contrasting elastic properties in generating changes in the effective normal stress at the mode-II margins of propagating ruptures. Perhaps the SAFOD rock property measurements can shed some light on this issue.

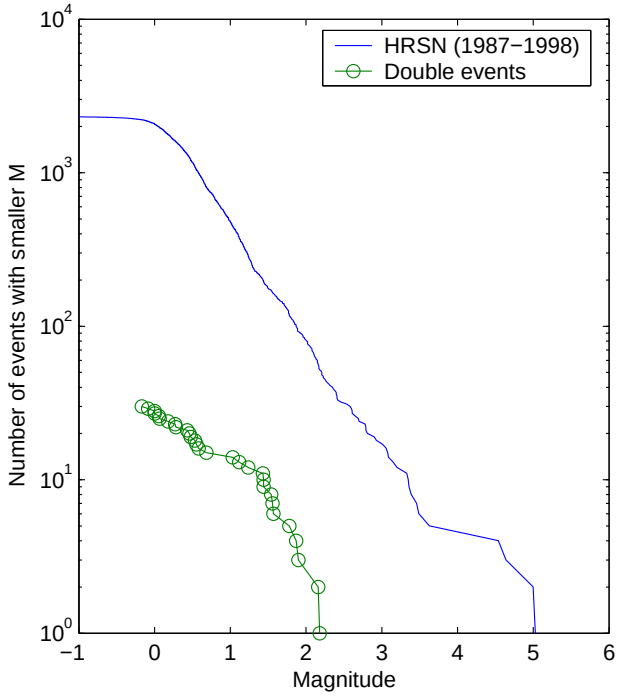

Figure 8: Magnitude-frequency distribution for the HRSN catalog (blue line) and those seismograms identified as compound (green).

Compound earthquake/immediate aftershock detection and relocation

Using the techniques outlined in the DATA ANALYSIS section we identified 30 compound seismograms with inter-event delay times of between ∼10 and 500 ms. These events have a magnitude-frequency distribution similar to that of the catalog as a whole (Figure 8). Delays shorter than 10 ms (5 samples) are hard to detect on the STFs due to the finite width of the peaks. In the future, these cases can be treated by using a triangular STF to fit the first (typically larger) peak (see Step 4). Due to the 10-sample window used to filter out spurious peaks in the STFs in Step 3, events separated by more than ∼50 m are less likely to be detected. For reference, an M1 earthquake has source radius of ∼15 m. The standard deviation of the residuals of relative location is less than half a sample (< 1 ms), but poor station coverage leads in some cases to location uncertainties larger than 10 m.

Figure 9 shows the space-time distribution of the 30 compound events, with the vertical axis being inter-event time and the horizontal axis the along-strike inter-event distance (negative values indicating that the 2nd event occurred to the NW of the first). For inter-event times longer than ∼30 ms, not much of a pattern emerges. There is a tendency for the mode-II aftershocks to occur to the NW, as in Figure 1 and unlike Figure 7, but the scatter is substantial and the error bars are a good

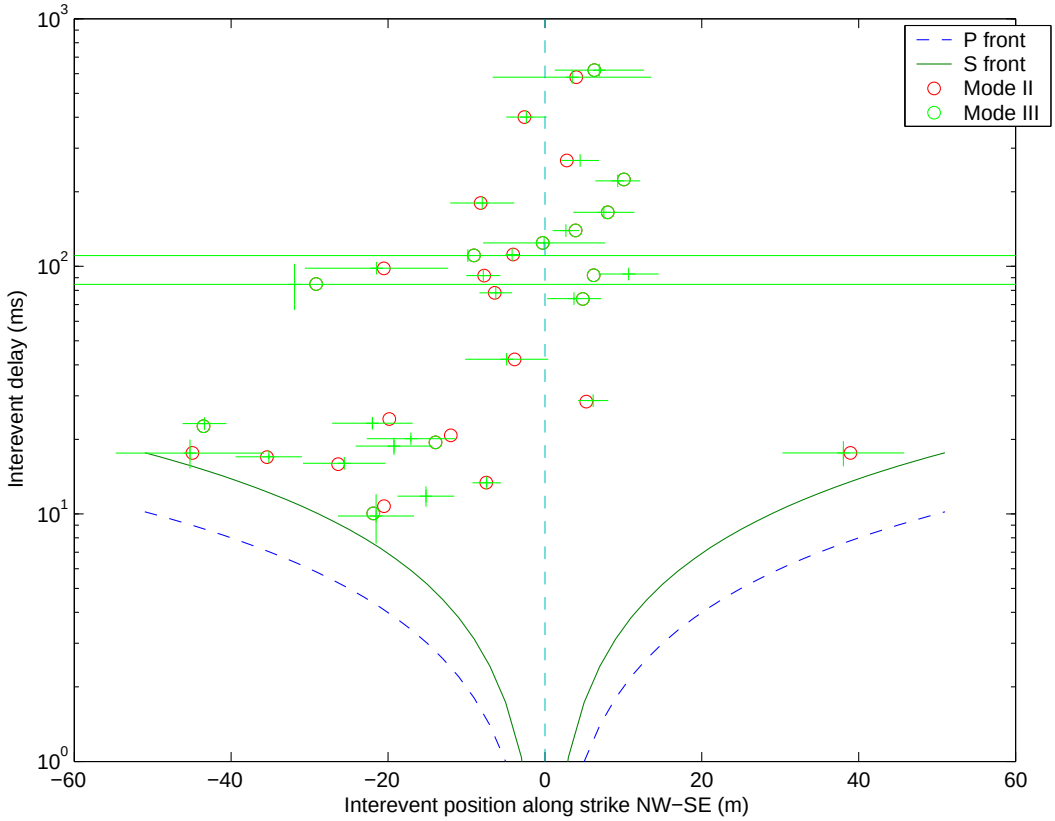

Figure 9: Inter-event time delay (vertical axis) vs. along-strike spatial separation (horizontal axis, negative values indicating the second sub-event being to the NW) for the identified compound earthquakes. Error bars (green lines) are equal to half the interquartile range taken from Monte-Carlo simulations.

fraction of the typical mainshock size (note that there is no obvious gap along strike corresponding to the rupture diameter). However, these aftershocks occur long after the passage of the seismic wave from the mainshock.

The most striking observation is that the distribution of the very earliest aftershocks is decidedly asymmetric, just as was the case for the long-term aftershocks in Figure 1. Of the 11 triggered events occurring within 30 ms, 8 occur beyond the mode-II margins of the "mainshock". Of these, 7 occur to the NW and only 1 to the SE. Many of these occur with an inter-event delay of roughly twice the S-wave travel time between centroids (solid green lines), and of these, many occur at an inter-event distance of roughly one source radius. This is consistent with triggering by the shear-wave arrival from the farthest mainshock crack tip.

To interpret this rather remarkable result we again turned to our numerical models. Figure 10 shows the time history of the change in Coulomb failure stress at various distances from the end of the numerical rupture in Figure 2b. The stars indicate when the rupture front would have arrived at the indicated point in the absence of stress barriers. Note that points just beyond the SE edge of the rupture experience their peak stress immediately upon arrest, but those to the NW experience increasing stresses on time scales comparable to the rupture duration. The reason is that the peak stress to the SE comes with the passage of the tensile stress pulse moving with the SE-propagating front, which is essentially instantaneous. In contrast, the peak stress to the NW occurs with the arrival of the stopping phases from the other edge of the crack. The implications of this are the following. A stress barrier to the SE either fails instantaneously or not at all. If it doesn't fail, it will not be detected. If it does fail, it will do so on a time scale that should make it nearly indistinguishable from continued propagation of the SE rupture front. In contrast, a barrier to the NW that fails may do so on the timescale of the stopping phases, making it clearly identifiable as a second event.

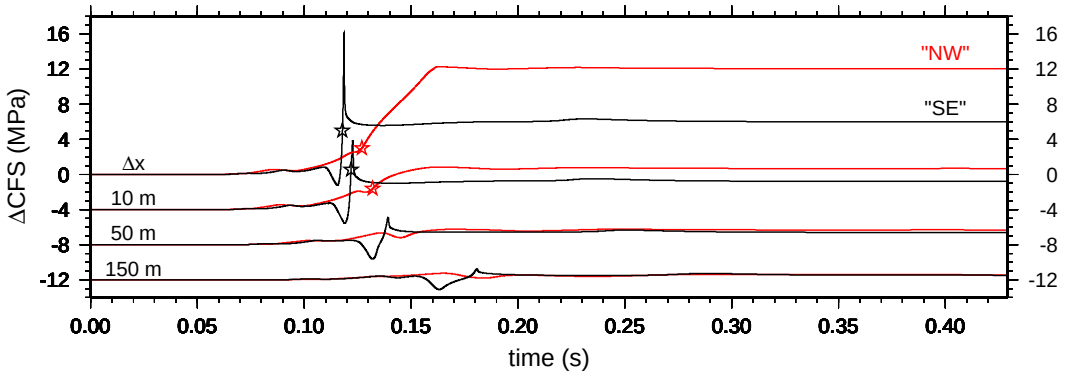

Figure 10: Time history of the change in Coulomb failure stress ΔCFS (defined as the change in shear stress plus the coefficient of friction times the change in normal stress, with tensile stresses positive) for the simulation of Figure 2b, at locations 1 gridpoint (0.125 m), 10 m, 50 m, and 150 m beyond the NW (red) and SE (black) ends of the rupture. Curves are offset along the vertical axis for clarity. Stars denote when the rupture front would have arrived at those points in the absence of stress barriers; it takes much longer to reach peak stress near the NW margin.

An important remaining goal is to verify that this observation is not an artifact of a bias in station coverage. While Figure 3 shows that the deconvovled earthquakes lie within the network, there is still a preponderance of stations to the SE. This means that a delayed subevent occurring to the SE would be more difficult to detect, as it would show up more readily on stations to the NW.

CONCLUSIONS

We examined the HRSN waveform catalog for compound events, and obtained relative locations and origin times by EGF deconvolution. Of the 2300 events examined, 11 had inter-event locations and origin times consistent with triggering during the dynamic phase of the mainshock, while stresses were still strongly time-varying. Of these, the vast majority occurred to the NW of the mainshock, consistent with the implications of numerical models of earthquake rupture on a bimaterial interface. That the sense of the long-term aftershock asymmetry near Parkfield is opposite to that near San Juan Bautista, as seen in the NCSN catalog, remains to be explained. We are delaying publication of these results until we can ensure that our observations are not an artifact of a bias in station coverage.

Acknowledgments

Analysis of the HRSN data was carried out by Jean-Paul Ampuero while he was a post-doc at Princeton University. HRSN data was accessed via the Northern California Earthquake Data Center. Cliff Thurber provided the ray parameters from his 3-D velocity model, and Bob Nadeau provided his catalog of HRSN moment magnitudes.

References

Abercrombie, R. E. (1996), The magnitude-frequency distribution of earthquakes recorded with deep seismometers at Cajon Pass, southern California, *Tectonophsys.*, *261*, 1–7.

McGuire, J. J., and Y. Ben-Zion (2005), High-resolution imaging of the Bear Valley section of the San Andreas fault at seismogenic depths with fault-zone head waves and relocated seismicity, *Geophys. J. Int.*, *163*, 152–164, doi:10.1111/j.1365-246X.2005.02703.x.

Rubin, A. M. (2002), Aftershocks of microearthquakes as probes of the mechanics of rupture, *J. Geophys. Res.*, *107*, 2142, doi:10.1029/2001JB000496.

Rubin, A. M. (2002b), Using repeating earthquakes to correct high-precision earthquake catalogs for time-dependent station delays, *Bull. Seism. Soc. Am.*, *92*, 1647–1659.

Rubin, A. M., and J.-P. Ampuero, (2007), Aftershock asymmetry on a bimaterial interface, *J. Geophys. Res.*, *112*, B11312, doi:10.1029/2005JB003686.

Rudnicki, J. W., and J. R. Rice (2006), Effective normal stress alteration due to pore pressure changes induced by dynamic slip propagation on a plane between dissimilar materials, *J. Geophys. Res.*, *111*, B10308, doi:10.1029/2001JB000496.

Thurber, C., H.J. Zhang, F. Waldhauser, J. Hardebeck, A. Michael, and D. Eberhart-Phillips (2006), Three-dimensional compressional wavespeed model, earthquake relocations, and focal mechanisms for the Parkfield, California region, *Bull. Seism. Soc. Am.*, *96*, S38–S49i Part B Suppl. S.

Weertman, J. (1980), Unstable slippage across a fault that separates elastic media of different elastic constants, *J. Geophys. Res.*, *85*, 1455–1461.

BIBLIOGRAPHY OF PUBLICATIONS RESULTING FROM THIS WORK

Ampuero, J.-P., and A.M. Rubin (2003), EGF search for compound source time functions in microearthquakes, Eos Trans. AGU, 84(46), Fall Meet. Suppl., Abstract S52H-02.

Ampuero, J.-P., and A.M. Rubin (2004), Constraints on dynamic triggering from very short term microearthquake aftershocks at Parkfield, Eos Trans. AGU, 85(47), Fall Meet. Suppl., Abstract S24A-08.

Ampuero, J.-P., and A.M. Rubin (2004), Dynamic triggering and asymmetry of immediate microearthquake aftershocks at Parkfield, SCEC annual meeting.